RSC Advances

PAPER

View Article Online
View Journal | View Issue

Cite this: *RSC Adv.*, 2025, **15**, 49388

Insight into the electronic, optical, and thermoelectric properties of novel ternary chalcohalides: next-generation energy applications

Muhammad Salman Khan, *[ac] Ayed M. Binzowaimil,[b] Catherine Stampfl,[c] Fahmida Fakhera,[c] Oliver J. Conquest,[c] Mohannad Al-Hmoud[b] and Siti Maisarah Aziz[d]

Received 3rd November 2025
Accepted 6th December 2025

DOI: 10.1039/d5ra08449k

rsc.li/rsc-advances

Due to their unique electronic structures and adjustable physical properties, ternary chalcohalides semiconductors are a class of materials with great potential for next-generation optoelectronic and thermoelectric applications. In this work, we examined the electronic, optical, and thermoelectric transport properties, along with the cohesive and formation energies of novel YSeM (M = Cl, Br) ternary chalcohalides using density functional theory. Both materials are found to be direct band gap materials having band gaps of 1.76 eV and 1.56 eV for YSeCl and YSeBr, respectively, using the PBE-GGA. Also, the band gaps obtained using the HSE06 are 2.69 eV and 2.18 eV, respectively. The sharp peaks in the reflectivity suggest these materials as active ultraviolet-reflecting materials and can be used in the ultraviolet protection applications. The negative Seebeck coefficient of these materials reveals that they show n-type conductivity. Due to their direct band gap nature and desirable thermal performance, they appear to hold considerable potential for applications in an extensive range of cutting-edge technologies.

1 Introduction

Ternary chalcohalides are promising materials for optoelectronic and thermoelectric applications due to the special mix of their structural characteristics and chemical bonding.[1,2] These materials have adjustable band gaps, which make them appropriate for light-emitting diodes, solar cells, and photodetectors where effective emission, light absorption, and charge carrier mobility are vital.[3] The combination of halogen and the chalcogen (S, Se, Te) elements balances the ionic and the covalent bonding, enhancing their optical performance such as their dielectric behaviour and high absorption coefficients.[4] Chalcohalide semiconductors also show great potential in the thermoelectric applications due to their poor heat conductivity, which is vital for their enhanced figure of merit value.[5] The electrically conducting properties of chalcohalides like the SbSI[6] and SbSeI[7] have been extensively investigated. To produce distinctive nanocrystalline SbSI directly, a novel sonochemical preparation technique has been developed.[8] Antimony selenoiodide (SbSeI), belonging to the same family, has been widely studied recently.[9–11] Vainshtein *et al.*[12] reported that SbSeI has an indirect band gap between the S and Γ high symmetry points, having a band gap of 1.66 eV, comparable to the experimental value (1.72 eV). Nitsche *et al.*[13] studied the photoelectric properties of SbTeBr, SbTeI, and SbSeI materials. Moreover, Kichambare *et al.*[14] produced SbTeI and estimated the lattice parameters, activation energy, energy band gap, and ionization energy at different temperatures. Additionally, Papazoglou *et al.*[15] conducted extensive research on the physical properties of SbTeI, concluding that SbSI was semiconducting. The Sb-based ternary chalcohalides can display a range of energy band gaps, which opens up promising possibilities for applications in batteries, memory, photoelectrical devices, and microprocessors.[16–18] Based on density functional theory (DFT) calculations, Bafekry *et al.*[19] predicted that the band gaps for two-dimensional (2D) SbSeI, SbSeBr, SbTeI, and SbTeBr, and thus the materials were considered attractive to be used in potential nanotechnology applications, in particular for optical applications.

The processes of SbSeI formation in single crystals by vapour phase approaches have also been reported.[20] The potential of SbSeI as X-ray and γ-ray detectors was examined by Wibowo *et al.*[21] The results suggest that SbSeI could be a promising semiconducting material for high-efficiency γ- and X-ray detection. The semi-conducting single-layer chalcohalides (BiChX) with Ch = S, Se, Te, and X = F, I, Br, and Cl[22] have drawn interest due to their Janus structures, which are produced as a consequence of the symmetry-breaking. The promising features of these materials include inherent polarized electrical fields,[23] piezoelectric potential,[24,25] and considerable Rashba

[a]*Department of Physics, Abdul Wali Khan University, Mardan, 23200, Pakistan. E-mail: salmankhan73030@gmail.com*

[b]*Department of Physics, College of Science, Imam Mohammad Ibn Saud Islamic University (IMSIU), Riyadh, 13318, Saudi Arabia*

[c]*School of Physics, The University of Sydney, Sydney, New South Wales 2006, Australia*

[d]*UniSZA Science and Medicine Foundation Centre, Universiti Sultan Zainal Abidin, Gong Badak Campus, 21300 Kuala Nerus, Terengganu, Malaysia*

spin-splitting.[26] Properties related to atomic structure, vibrations, elasticity, piezoelectricity, and electricity of BiChX monolayers (Ch = S, Se, Te; X = F, I, Br, Cl) were investigated by Varjovi *et al.*[24] The dynamic stability of the Bi-based ternary chalcohalides using *ab initio* simulations of molecular dynamics up to 600 K and vibrational frequency analysis was demonstrated.[27] It was anticipated that Bi-based ternary chalcohalide, in particular, responds favourably in the visible light spectrum,[27] and was investigated for solar energy harvesting. Some iso-structural materials, such as BiSeCl, BiSeI, and BiSeBr, demonstrate optical band gap values in the range 1.47–1.48 eV. The electron or hole effective masses in BiSCl, BiSBr, and BiSI materials are less than m_o, indicating that these materials could be suitable for detecting room temperature (RT) radiation.[28] SbSI possesses an optical band gap value of ~2.0 eV.[29] The estimated theoretical electron effective masses for SbSI, SbSBr, and SbSeI obtained using the generalized gradient approximation (GGA) were reported to be 0.21, 0.26, and 0.52 m_0, respectively, which indicates the possibility of high mobility with low defect concentrations.[30]

The introduction of Se reduces the energy gap largely because of the changes in the lattice properties, where adding Se to BiSI changes the indirect band gap between 1.63 and 1.48 eV.[31] Ganose *et al.*[32] investigated the BiSeI and BiSI compounds using the relativistic hybrid DFT approach and including spin–orbit coupling to demonstrate their potential use in photovoltaic devices. Later on, they also explored the optoelectronic features of the compounds with the quasiparticle self-consistent GW (QSGW) approach.[33] The predicted band gap value for BiSI was 1.76 eV, and for BiSeI, it was 1.50 eV, which is in close agreement with their previous hybrid DFT prediction.[33] Ran *et al.*[34] calculated the electronic properties of the BiSCl and BiSeCl and revealed that they have indirect band gaps ranges from 1.0–1.7 eV. Luo *et al.*[35] observed that the Janus single-layer ternary chalcohalides have remarkable fluctuating, temperature-dependent, and a good mechanical stability. To achieve the effective use of the solar energy, a more detailed theoretical investigation ranging into the physical features of the ternary YSeM (M = Cl, Br) chalcohalides is needed. The knowledge of the electronic properties, like the band structures, also offers significant insight into a material's potential performance, which is vital for its use in the electronic devices. Investigating the thermoelectric properties can further result in the advancement of the active thermoelectric materials, which are essential for the energy conversion technologies.

2 Computational method

The Vienna *Ab initio* Simulation Package (VASP)[36,37] is employed to perform the present calculations based on the Density Functional Theory (DFT). Electron interactions were described by the Perdew Burke Ernzerhof Generalized Gradient Approximation (PBE-GGA).[38] It is well known that the PBE-GGA underestimates the band gap, so for the band structure calculations, the more accurate Heyd–Scuseria–Ernzerhof (HSE06) hybrid functional[39] is used. Here, a portion of Hartree–Fock theory's precise exchange is incorporated into HSE06, enhancing the accuracy of the energy band gap predictions and significantly improving the optoelectronic properties. We used the VASP package to calculate the dielectric function from which the absorption coefficient and refractive index can be evaluated. To assure accuracy, the *k*-point mesh for the Brillouin zone sampling and plane-wave cutoff energy were tested to establish the basis set. A Γ-centered *k*-mesh of 11 × 11 × 11 using the Monkhorst–Pack method was employed. For the self-consistent and structural optimization, the energy convergence was set to 10^{-5} eV and the force convergence to 0.01 eV $Å^{-1}$. The HSE06 hybrid functional, instead of the PBE, was employed for calculating all optical parameters. HSE06 was selected specifically for its more precise band gap and the electronic structure, which directly increases the dependability of the obtained optical spectra. We employed DFT using the random phase approximation (RPA), which only includes local field effects at the Hartree level, to determine the optical characteristics. For these optical properties calculations, we used an 11 × 11 × 11 *k*-point set, and 900 unoccupied bands were both of these parameters to yield convergence. The imaginary part of the dielectric function is obtained from the interband transitions evaluated using momentum-matrix elements between the Kohn–Sham states on a dense *k*-point mesh, while explaining how the real component is subsequently calculated using the Kramers–Kronig relationship which are expressed as:[40]

$$\varepsilon_1(\omega) = 1 + \frac{2}{\pi} p \int_0^{\infty} \frac{\omega' \varepsilon_2\left(\omega'\right) \mathrm{d}\omega'}{\omega'^2 - \omega^2} \tag{1}$$

$$\varepsilon_2(\omega) = \left(\frac{4\pi^2 e^2}{m^2\omega^2}\right) \sum_{i,j} \int \langle i|M|j\rangle^2 f_i(1-f_i) \times \ \delta\left(E_f - E_i \ - \omega\right) d^3k \tag{2}$$

In eqn (1), "*p*" represents the Cauchy principal integral value, $\omega'\varepsilon_2(\omega')$ denotes the absorptive response of material, and $\frac{1}{\omega'^2 - \omega^2}$ represents the dispersion relation. Likewise, in eqn (2), in $\left(\frac{4\pi^2 e^2}{m^2\omega^2}\right)$, m represents the mass of the electron, e represents the elementary charge, and ω is the incident light angular frequency. Similalry, the term $i|M|j^2$ signifies the square of dipole matrix element. The following optical properties are obtained using the real and imaginary components and are expressed as:

$$L(\omega) = \frac{\varepsilon_2(\omega)}{\varepsilon_1{}^2(\omega) + \varepsilon_2{}^2(\omega)} \tag{3}$$

$$I(\omega) = \frac{\sqrt{2}\omega}{c}\left(\sqrt{\left(\varepsilon_1{}^2(\omega) + \varepsilon_2{}^2(\omega)\right)} - \varepsilon_1(\omega)\right)^{\frac{1}{2}} \tag{4}$$

$$n(\omega) = \left(\frac{1}{2}\left[\sqrt{\left(\varepsilon_1{}^2(\omega) + \varepsilon_2{}^2(\omega)\right)} + \varepsilon_1(\omega)\right]\right)^{\frac{1}{2}} \tag{5}$$

$$R(\omega) = \left|\frac{\sqrt{\varepsilon(\omega)} - 1}{\sqrt{\varepsilon(\omega)} + 1}\right|^2 \tag{6}$$

The BoltzTraP computational tool was used for the thermoelectric calculations. These thermoelectric properties were calculated by employing Onsager's expressions and Boltzmann's transport theory:[41]

$$\vec{J} = \sigma E_O - \sigma S \nabla T \quad (7)$$

$$\vec{J} = \sigma S T E_O - \kappa \nabla T \quad (8)$$

$$ZT = \frac{S^2 \sigma T}{\kappa} \quad (9)$$

Here the σ, E_O, ∇T, S, κ, ZT, and $\vec{J}$ are the electric conductivity, the external electric field, the temperature gradients, the Seebeck coefficient, thermal conductivity, the figure of merit, and the electrical current density, respectively.

3 Results and discussion

3.1 Structural properties

The structure of the ternary chalcohalides YSeM (M = Cl, Br) crystallize in the cubic $F\bar{4}3m$ space group (no. 216) (see Fig. 1). Dark blue spheres show Yttrium (Y) atoms; they occupy high-symmetry positions within the unit cell. The Y atoms are located at the unit cell's corners and face centres. Y^{3+} forms distorted YSe_4Cl_6 tetrahedra bonded with four Se^{2-} atoms and six Cl^{1-} atoms. These tetrahedra share six YSe_4Cl_6 tetrahedra, six ClY_6Se_4 tetrahedra on their edges, and twelve YSe_4Cl_6 tetrahedra on their faces. Each of the Y–Se bonds has a length of 2.97 Å. Each of the Y–Cl bonds has a length of 3.43 Å. Se^{2-} is bonded to four Y^{3+} and four Cl^{3-} atoms in a body-centred cubic lattice. The Se–Cl bond lengths are all 2.97 Å. Cl^{1-} forms ClY_6Se_4 tetrahedra that share corners with four YSe_4Cl_6 tetrahedra. Moreover, Cl^{1-} atoms are bonded to six Y^{3+} and four Se^{2-} atoms. In the YSeBr structure, the Y^{3+} is bonded to four comparable Se^{2-} and six comparable Br^{1-} atoms, resulting in YSe_4Br_6 tetrahedra having deformed faces and shared edges. Br^{1-} is confined in a ten-coordinate geometry with six comparable Y^{3+} and four comparable atoms of Se^{2-}. Table 1 shows that our computed lattice constants a, b, and c agree well with earlier literature values, illustrating the structural dependability of our results. The cohesive energy has a substantial influence on the stability and the phase transition characteristics. The calculated cohesive energies are obtained by using the relation:[26]

$$E_{coh} = E(\mathrm{YSeM}) - mE(\mathrm{Y_{atom}}) - nE(\mathrm{Se_{atom}}) - pE(\mathrm{M_{atom}}) \quad (10)$$

here $E(\mathrm{Y_{atom}})$, $E(\mathrm{Se_{atom}})$, and $E(\mathrm{M_{atom}})$ denote the total energy of Y, Se, and M free atoms and E(YSeM) is the total energy of the YSeM system and m, n, and p are the number of Y, Se, and M atoms in the unit cell. The YSeCl and YSeBr have calculated cohesive energy of −3.76 eV per atom and −2.28 eV per atom, respectively. As demonstrated in Table 1, the calculated cohesive energies are congruent with published data, showing consistent bonding strength predictions across investigations. A larger negative cohesive energy indicates stronger bonding inside the material, requiring more energy to break the bonds. Stronger bonding is usually linked with a larger band gap, as strongly bonded atoms have more separated electronic states, resulting in a wider gap between the valence and conduction bands.[42] Similarly, YSeCl has a wider band gap than YSeBr, as confirmed by the calculated band structure. Formation energy is frequently regarded as the primary and satisfactory indication for determining whether the material is stable against disintegration into its basic components or in their competing phases.

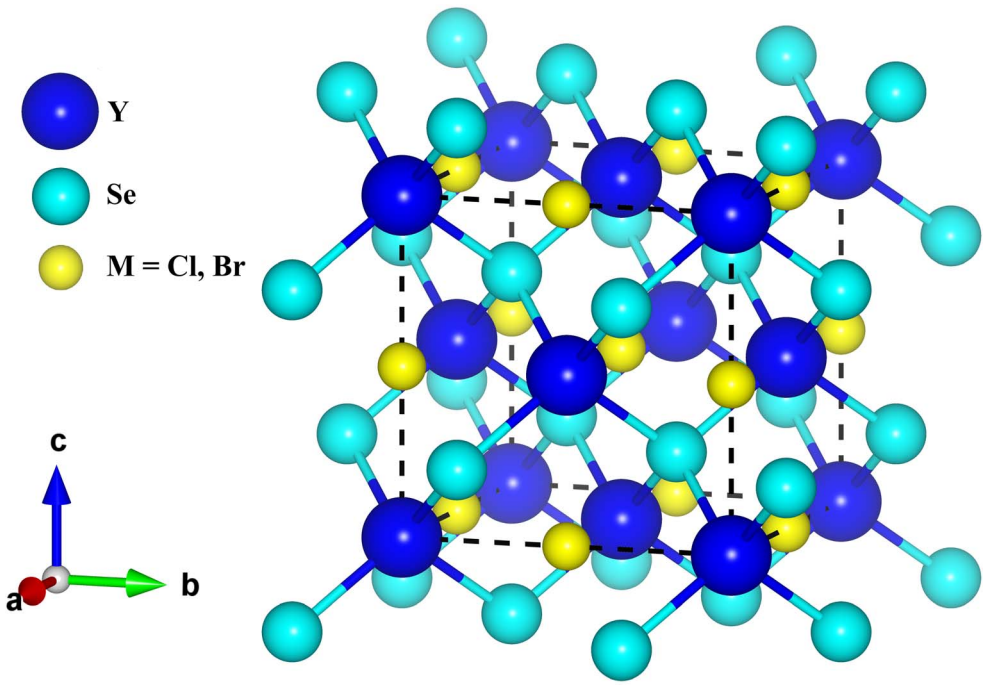

Fig. 1 The unit cell crystal structure of YSeM (M = Cl, Br) ternary chalcohalides.

Table 1 The lattice constants, cohesive, formation energies and band gaps for YSeM (M = Cl, Br) ternary chalcohalides

Materials	a(Å)	b(Å)	c(Å)	E_{coh} eV per atom	E_{form} (eV f.u.$^{-1}$)	E_g (eV) PBE-GGA	E_g (eV) HSE06
YSeCl (this work)	4.29	4.29	4.29	−3.76	−2.37	1.76	2.69
YSeBr (this work)	4.12	4.12	4.12	−2.28		1.56	
SbSeBr	4.01[a]	4.01[a]	4.01[a]	−2.90[a]		1.25[a]	
SbTeBr	4.24[a]	4.24[a]	4.24[a]	−2.78[a]		1.51[a]	
BiSeCl	4.15[b]	4.15[b]	4.15[b]	2.92[b]		1.65[b]	
BiSeBr	4.19[b]	4.19[b]	4.19[b]	2.77[b]		1.56[b]	
BiSeI	4.27[b]	4.27[b]	4.27[b]	2.61[b]		1.63[b]	
BiSCl	4.06[b]	4.06[b]	4.06[b]				
BiSBr	4.11[b]	4.11[b]	4.11[b]	3.06[b]	−2.23	1.80[b]	2.18
BiTeCl	4.31[b]	4.31[b]	4.31[b]				
BiTeBr	4.35[b]	4.35[b]	4.35[b]	2.90[b]		1.77[b]	
TiClS	3.47[c]	3.47[c]	3.47[c]				
TiClSe	3.58[c]	3.58[c]	3.58[c]	2.77[b]		1.77[b]	
TiClTe	3.65[c]	3.65[c]	3.65[c]				
BiTeBr	4.35[d]	4.35[d]	7.06[d]	2.62[b]		1.60[b]	
BiTeCl	4.29[d]	4.29[d]	13.34[d]				

[a] Ref. 19. [b] Ref. 24. [c] Ref. 44. [d] Ref. 46.

The computed formation energies for YSeCl and YSeBr are −2.37 eV f.u.$^{-1}$ and −2.23 eV f.u.$^{-1}$, respectively (see Table 1). Both phases are thermodynamically favourable with respect to their elemental constituents. YSeCl is slightly more stable by ∼0.14 eV per formula unit, which indicates stronger net bonding and a higher energetic cost for decomposition. Chemically, this trend is consistent with the halogen impact: chloride's lower ionic radius and stronger electronegativity improve bond polarity and strengthen Y–Cl and Se–Cl bonds as compared to larger, less electronegative bromide, leading to a deeper formation energy for YSeCl. Yttrium in the +3 oxidation state provides charge balance and compact coordination, stabilizing the mixed-anion framework, while selenium's p-states dominate the valence-band edge and participate in covalent bonding, influencing cohesion and electronic structure; the halogen notably tunes lattice cohesion and bond polarity, influencing both cohesive energy and formation energy. While these formation energies give strong basic evidence of synthesizability and relative stability of YSeCl being the more stable choice, further testing against competing phases and dynamical stability is required to make definitive conclusions. A comprehensive evaluation of the different phases and phonon-based dynamical stability is computationally expensive because it requires extensive phase-space search and high-precision supercell phonon computations, which substantially raise total calculation time and resources.

3.2 Electronic properties

The electronic band structure of the YSeM (M = Cl, Br) materials was calculated using the PBE-GGA and HSE06 functionals, where the HSE06 functional generates a larger and more accurate band gap than the PBE-GGA. The valence band maximum and the conduction band minimum, as illustrated in Fig. 2(a–d), are located at the Γ-point in the Brillouin zone, which confirms direct band gaps. The band gap values of YSeCl and YSeBr obtained through the PBE-GGA are 1.76 eV, and 1.56 eV respectively, and using the HSE06, the predicted values are 2.69 eV and 2.18 eV, respectively. The PBE-GGA band gaps in Table 1 exhibit excellent agreement with published values, indicating the accuracy of our electronic structure calculation methods. In the PBE-GGA, the electron–electron interactions are approximated, which leads to self-interaction errors resulting in the underestimation of the energy gap values. The HSE06 includes a component of a precise exchange, which better accounts for electron–electron repulsion. This modifies the delocalization and minimizes self-interaction problems, giving more accurate band gaps. Additionally, the HSE06 uses a kind of screened Coulomb potential that restricts the range of exact exchange–correlation interaction and allows it to describe short- and long-range electronic correlations more precisely than the PBE-GGA. A primary consideration for selecting materials for the optoelectronic applications is the band gap value, which is vital in determining their suitability for devices such as the solar cells, and the photodetectors. The YSeCl material appears more suitable for the optoelectronic devices because of its somewhat wider band gap and is also potentially of interest for the applications demanding an effective electron–hole pair production and the recombination. The large band gap of the YSeCl could also make it suitable for the visible light-emitting applications. It is noted that the band gaps are also influenced by the atomic size and the electronegativity of the constituent atoms in the materials. Chlorine, in the YSeCl, is more electronegative and smaller than bromine in YSeBr, which results in a large band gap. Selenium improves intermediate bond strength and the electron affinity, consequential for the band gaps appropriate for the optoelectronic applications. In contrast, YSeBr's smaller band gap, because of bromine's lower electronegativity and large atomic radius, could make it appropriate for applications requiring lower-energy photon absorption. Consequently, the choice between YSeCl and YSeBr is determined by the explicit optoelectronic application; however, YSeCl's wider band gap would make it more compliant

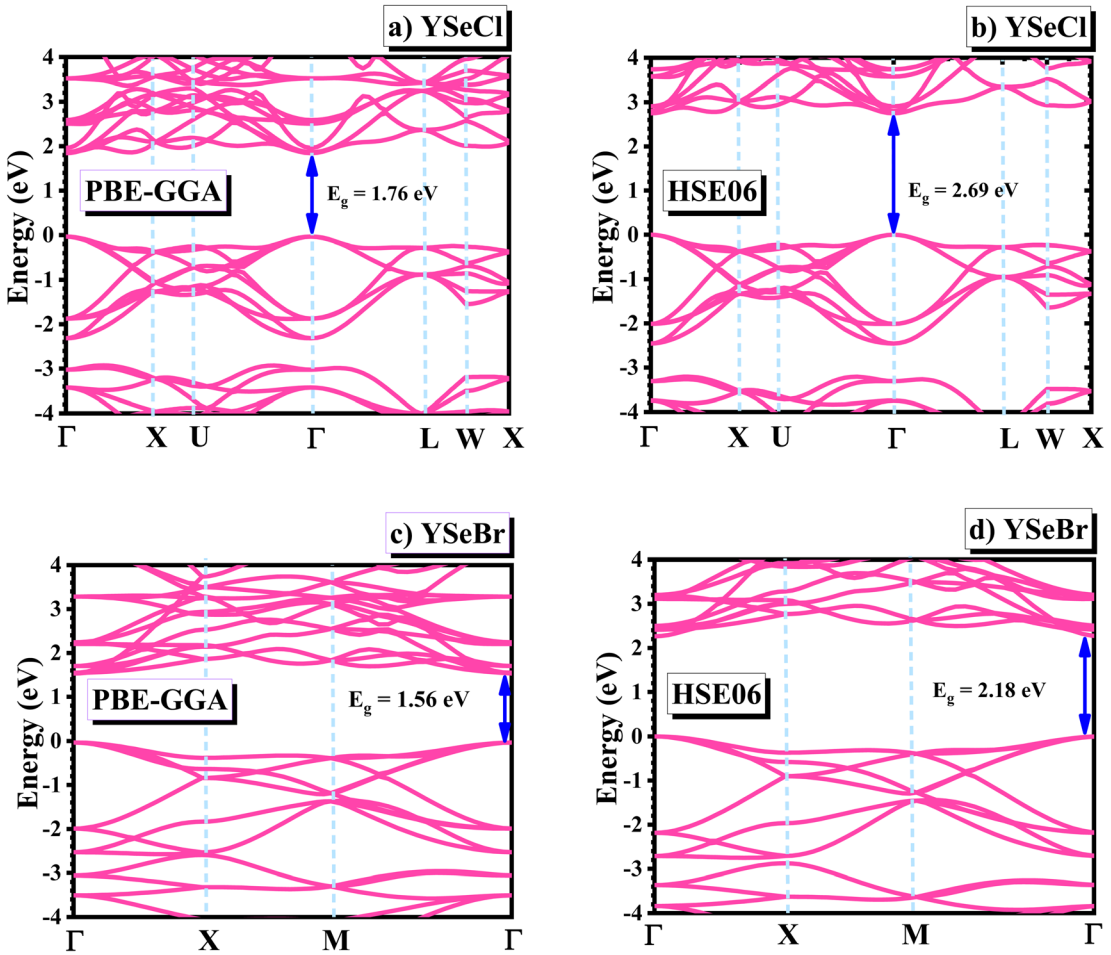

Fig. 2 The calculated band structure with PBE-GGA and HSE06, for the (a and b) YSeCl and (c and d) YSeBr ternary chalcohalides.

for higher-energy applications. The contributions of different electronic states to the valence band are determined by the bonding nature of atoms, the types of orbitals involved, and their interactions. The various contributions can be seen from the density of states (DOS) shown in Fig. 3. Y-s orbitals form bonding states closer to the Fermi level. The states −4.5 eV and the Fermi level have a significant impact on the material's bonding properties. The Y-d orbitals are more localized than the s orbital; therefore, they overlap less effectively with the orbitals of neighbouring atoms. The Se, Cl, and Br are relatively electronegative, and their p orbitals, which are more delocalized than the d orbitals, participate in bonding and can contribute considerably in the valence band uppermost region.

Transition metals often have high-energy d orbitals that contribute to conduction, and it can be seen that the Y-d orbitals dominate in the conduction band lower region, ranges 2.0 eV to 4.5 eV. At higher energies between 4.5 eV to 6.0 eV, the Y-s orbitals become more prominent and are broader and delocalized. The Se- and Br-p states contribute from 1.8 eV to 5.5 eV, demonstrating their involvement in the bonding environment and electronic states that extend into the conduction band. It can be seen from the DOS in Fig. 3 that the two materials have similar contributions from the respective atomic orbitals. Because s orbitals are more delocalized than the p and d they extend across most of the energy of the valence band. It can be noted that there is hybridization of the Y s-states with the p-states of the other elements just below the Fermi level. The minimal contribution of Y-d orbitals in the same energy range may be explained by the higher energy and generally more localized nature of the d orbitals, which implies that they contribute less to bonding. The Se, Cl, and Br p states contribute more near the Fermi level. The p states usually form bonding and anti-bonding states in materials. The Y-s and Y-p orbitals, as well as the Cl-p and Br-s/d states, contributed less to the conduction band from 2.0 eV to 4.5 eV. The Y-6s orbital can be seen at around 4.5 eV to 6.0 eV, and p states of Se and Br contribute between 1.8 eV and 5.5 eV. The Se- and Br-p orbitals significantly contribute to the bonding as they are more electronegative elements and establish bonding states in the valence band region and anti-bonding in the unoccupied region.

3.3 Optical properties

The important optical properties of the YSeCl and YSeBr semiconductors, including their complex dielectric functions, were calculated to assess their possible optical applications. The ability of a material to polarize due to an applied static electric field is indicated by the static dielectric constant $\varepsilon_1(0)$ at zero frequency, as shown in Fig. 4(a). The $\varepsilon_1(0)$ static values for YSeCl

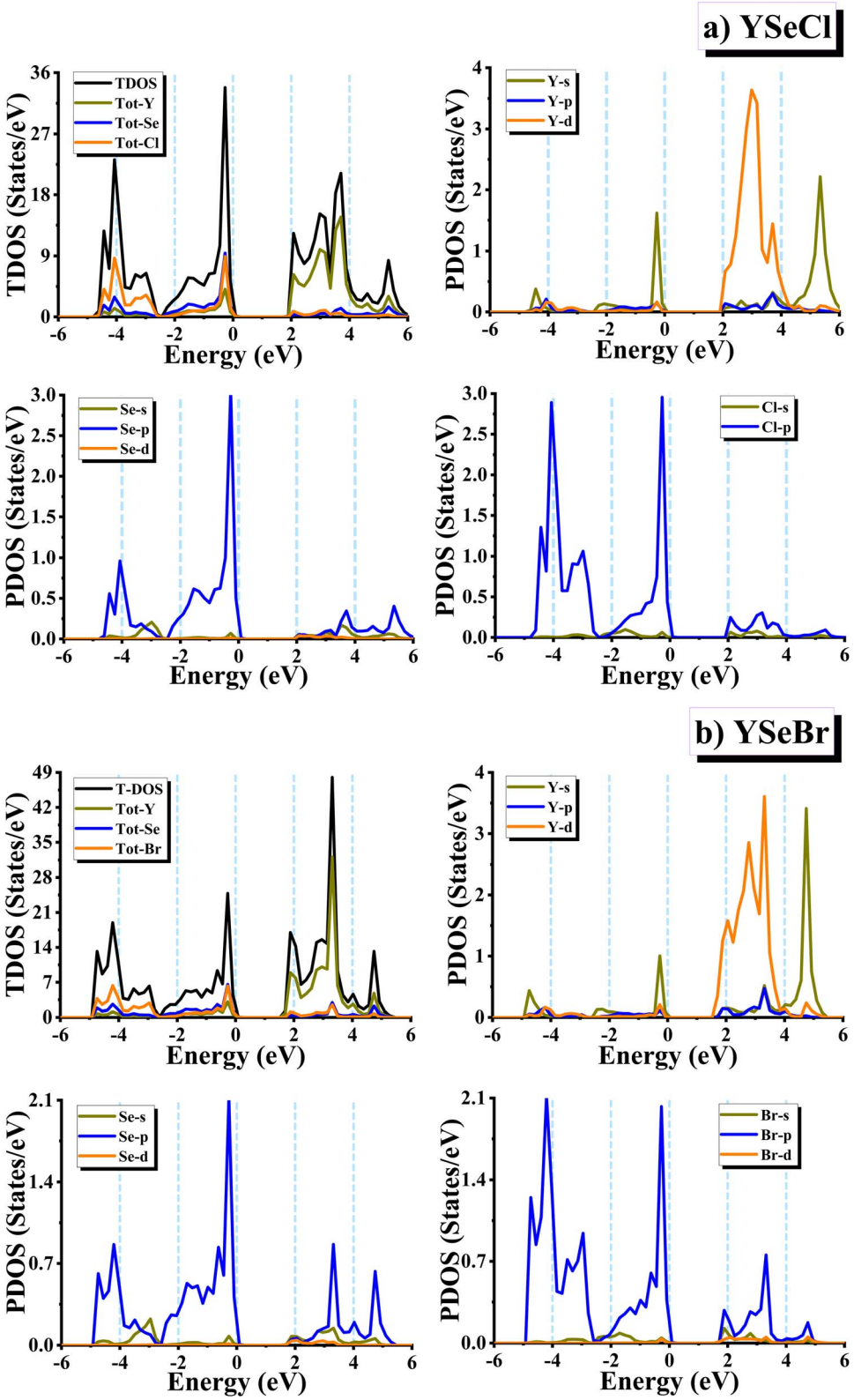

Fig. 3 The calculated total and orbital projected density of states for (a) YSeCl and (b) YSeBr ternary chalcohalides.

and YSeBr are 8.5 and 10.5, respectively, showing that YSeBr is somewhat more polarized than YSeCl. Table 2 shows our calculated static actual dielectric constants accord well with the corresponding literature values, validating the reliability of our optical predictions. The real dielectric function $\varepsilon_1(\omega)$ rises with an increase in the photon energy and approaches to a peak value at 2.2 eV for YSeCl and 2.0 eV for YSeBr. With an increase in photon energy, electrons can no longer effectively screen the

external field, resulting in a reduction in $\varepsilon_1(\omega)$ and finally acquiring negative values. The precise frequency at which this occurs (6.8 eV for YSeCl and 6.6 eV for YSeBr) suggests that both materials have similar high-energy electronic structures that result in plasmonic activity at these frequencies. For photon energy greater than 2.0 eV, the value of the real component decreases and varies. For energies below 2.0 eV, YSeBr exhibits a somewhat greater peak in the $\varepsilon_1(\omega)$ compared to YSeCl; nonetheless, both compounds exhibit very similar behaviour for energies greater than about 8.5 eV. The dielectric response of a material that is dissipative (absorptive) is represented by the imaginary component, $\varepsilon_2(\omega)$, as shown in Fig. 4(b). With sharp peaks at around 2–3 eV and a subsequent decline at higher energy, both materials' performances are somewhat comparable. The electronic transitions that occur when the material absorbs energy and electrons are excited to higher energy states are linked to these sharp peaks. Compared to YSeCl, YSeBr exhibits somewhat greater absorption at low energies; but at higher energies, especially over 9.0 eV, the two materials respond essentially identically. For YSeCl, $\varepsilon_2(\omega)$ starts its sharp increase at 1.8 eV, while for YSeBr, it begins at 1.7 eV and is consistent with the band gap values. For YSeCl and YSeBr, $\varepsilon_2(\omega)$ reaches its highest value at around 2.2 eV and subsequently declines as the photon energy increases. For an increase in photon energy, the likelihood of finding electrons in the valence band that can be excited by higher-energy photons decreases. Since higher-energy photons have a lower absorption probability, the imaginary part decreases.

Table 2 The computed static values of dielectric real component, refractive index, and reflectivity values for YSeM (M = Cl, Br) ternary chalcohalides

Materials	$\varepsilon_1(0)$	$n(0)$	$R(0)$
YSeCl (this work)	8.5	2.9	0.25
YSeBr (this work)	10.5		
SbSeBr	5.0[a]		
SbSeI	5.5[a]		
SbTeBr	5.7[a]		
SbTeI	6.0[a]	3.2	0.28
BiTeI	12.5[b]		
BiTeBr	13.5[b]		
BiTeCl	10.5[b]		
SbTeI	11.0[b]		

[a] Ref. 19. [b] Ref. 46.

The refractive index, $n(\omega)$, defines how light propagates through a material and is closely related to the dielectric function, specifically with the $\varepsilon_1(\omega)$. According to Fig. 4(c), for YSeCl, the value of $n(0)$ is 2.9, and for YSeBr, it is 3.2 (see Table 2),

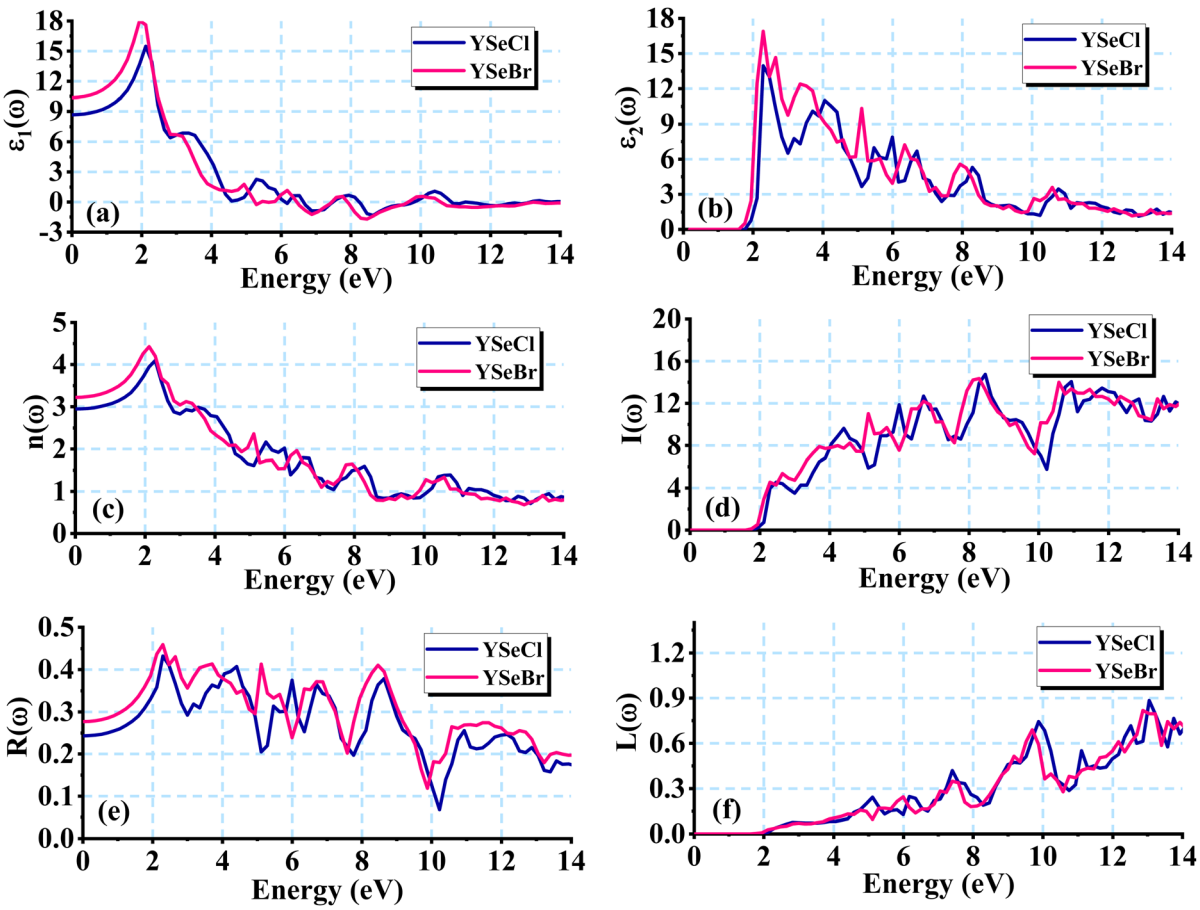

Fig. 4 The calculated (a) real dielectric constant, (b) imaginary dielectric constant, (c) refractive index, (d) absorption coefficient, (e) reflectivity spectra, (f) energy loss function, for YSeM (M = Cl, Br) ternary chalcohalides.

suggesting that YSeBr would bend light more than YSeCl under static conditions. The refractive indices of YSeCl and YSeBr peak at about 2.4 eV, then decrease with increasing energy. Light is slowed down significantly by YSeBr as compared to YSeCl at lower energy, as indicated by its higher refractive index. At energies above 6.0 eV, there is not much difference between the two materials. The sharp initial peak occurs earlier for the YSeBr, implying that the electronic structure of the YSeBr allows interband transitions to occur at slightly lower energies than in the YSeCl. YSeBr has a greater maximum refractive index than YSeCl, which is dependable on its higher polarizability and the dielectric constant. With increasing photon energy, the refractive index decreases because the material's capacity to delay or bend light weakens with the increasing energy. As the photon energy increases, the refractive index $n(\omega)$ approaches unity at roughly 8.7 eV for both the YSeCl and YSeBr. A refractive index of 1 specifies that the material no longer slows or bends light, allowing the light to flow through it as it would in the vacuum. The absorption coefficient $I(\omega)$ is directly connected to the electronic transitions that occur when the material absorbs photons of a particular energy. From Fig. 4(d), the optical band gap is represented by the initial rise in the absorption coefficient from a threshold value of 1.9 eV for YSeCl and 1.8 eV for YSeBr. Following the peak at 8.6 eV, the absorption coefficient drops as the photon energy approaches 10.5 eV and 9.9 eV for YSeCl and YSeBr, respectively. This drop occurs because at higher energies, fewer transitions are available, or the available transitions entail states with lower oscillator strengths. Beyond 10.5 eV, the absorption of YSeCl and YSeBr increases again, most likely due to a new set of electronic transitions. The transitions may occur from the deeper valence states to conduction bands or could include more complicated mechanisms, such as excitons or core-level excitations. YSeBr displays slightly stronger absorption at low energy as compared to YSeCl, although both materials perform equivalently at high energies *i.e.*, from 10 eV and above. This shows that YSeBr may be somewhat more suitable for applications that require robust absorption at lower photon energies.

The dependence of the reflectivity on photon energy reveals how light interacts with the material's surface as well as internal electronic changes. In Fig. 4(e), the static reflectivity $R(0)$ for YSeCl is 0.25, while for YSeBr it is 0.28 (see Table 2). These results indicate that even at low frequencies, YSeBr reflects more light compared to the YSeCl. The difference in reflectivity is attributable to the YSeBr's greater refractive index and the dielectric constant compared to the YSeCl. The reflectivity increases with the photon energy $\hbar\omega$, reaching maximum values of 0.3 and 0.4 at 2.2 eV and 8.6 eV for both these materials. This rise in the reflectance indicates a significant light–matter interactions at these specific energies, which are often caused by the electronic transitions within these materials. The intense peaks in the calculated reflectivity indicate the potential employment of these materials as active UV-reflecting materials. At photon energies of about 10.0 eV, both the YSeCl and YSeBr show a considerable drop in the reflectivity. Fig. 4(f), reveals that the threshold for both the YSeCl and YSeBr is around 2.0 eV. Both materials show a peak between 9.0 and 12.0 eV, illustrating plasmon energy, wherein the electron density oscillates in response to the external electromagnetic fields. Another lower energy plasmon at 7.5 eV results in another peak in $L(\omega)$ and YSeBr loses somewhat more energy at lower energies (up to 8.0 eV), but both materials have identical plasmon peaks. This implies that they exhibit similar energy loss patterns at high photon energies. $L(\omega)$ decreases little beyond 10.0 eV, indicating plasmon excitation damping. Following an initial reduction, the energy loss function rises again, indicating the presence of higher-energy excitations.

3.4 Thermoelectric properties

The Seebeck coefficient is shown in Fig. 5(a). It can be seen that it decreases, which is because of the low carrier concentration, with thermopower being influenced by the energy disparity between the Fermi level and the transport energy levels. Negative Seebeck values for YSeCl and YSeBr suggest n-type behaviour, in which electrons are dominant charge carriers. From 50 K to 850 K, the Seebeck coefficient decreases linearly, becoming more negative as the temperature increases. Over the whole temperature range, YSeBr exhibits a less negative Seebeck coefficient than YSeCl, revealing that YSeCl could possess better thermoelectric performance because of the smaller magnitude of the Seebeck coefficient. This leads to a larger carrier concentration, which lowers the Seebeck coefficient. At 850 K, YSeBr has a smaller Seebeck coefficient (-6.5 μV K^{-1}) than YSeCl (-8.1 μV K^{-1}). At high temperatures, the lower vibrational frequency of YSeBr can lead to increased electron-phonon scattering.[43] Fig. 5(b) illustrates the variation of electrical conductivity for YSeCl and YSeBr from 50 K to 850 K. Table 3 shows how our computed electrical conductivity values at 300 K are consistent with those reported in the literature, supporting the reliability of our results. For both materials, electrical conductivity increases with temperature. At all temperatures, the electrical conductivity of YSeCl is greater than YSeBr, *e.g.* at 850 K, YSeBr has a value of 1.4×10^{18} $(\Omega\ \mathrm{ms})^{-1}$ and YSeCl has a value of 2.2×10^{18} $(\Omega\ \mathrm{ms})^{-1}$. Better electrical conductivity in YSeCl raises the possibility of improved carrier mobility or density. Although YSeCl and YSeBr have comparable lattice structures, the binding strength between the atoms varies. Chlorine (Cl) is smaller and more electronegative than bromine (Br), and YSeCl bonds are stronger and shorter than those in YSeBr, as confirmed by the calculated cohesive energy values. Stronger bonds in YSeCl lead to a more stable lattice structure and fewer phonon scattering events. Thermal excitation becomes more significant at the higher temperatures (850 K), allowing for the thermal activation of more charge carriers.

The thermal conductivity is depicted in Fig. 5(c). As shown in Table 3, the projected electronic thermal conductivity values at 300 K correspond well with the literature findings, confirming the precision of the present electronic transport evaluations. The electronic thermal conductivity of both materials rises linearly, suggesting that charge carriers are carrying more heat energy at high temperatures. Since lower thermal conductivity increases the thermoelectric figure of merit, YSeCl's slightly reduced thermal conductivity compared to YSeBr may be advantageous. The

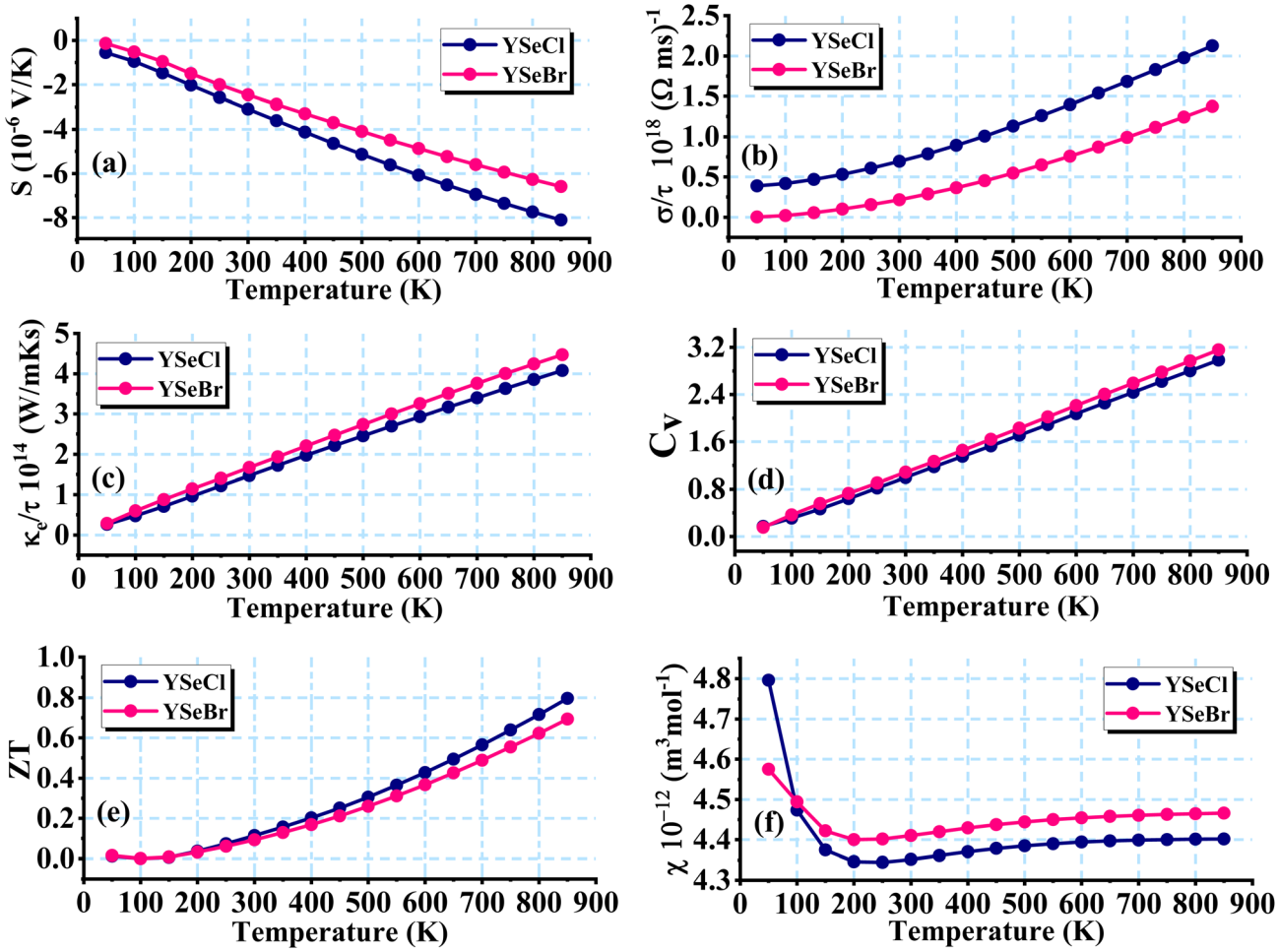

Fig. 5 The calculated (a) Seebeck coefficient, (b) electrical conductivity, (c) thermal conductivity, (d) specific heat capacity, (e) figure of Merit, and (f) electrical susceptibility, for YSeM (M = Cl, Br) ternary chalcohalides.

Table 3 The calculated electrical conductivity (σ/τ), electronic thermal conductivity (κ_e/τ), and figure of merit (ZT) at 300 K for YSeM (M = Cl, Br) ternary chalcohalides

Materials	(σ/τ) $\times 10^{18}$ (Ω ms)$^{-1}$	(κ_e/τ) $\times 10^{14}$ W mK s^{-1}	ZT
YSeCl (this work)	0.75	1.60	0.11
YSeBr (this work)	0.25	1.70	0.10
BiTeCl	1.70[b]	1.30[b]	0.43[a]
BiTeBr	0.70[b]	0.70[b]	
SbSeBr	1.80[b]	1.70[b]	0.70[a]
SbSeI	0.80[b]	0.80[b]	
SbTeBr	0.60[c]	1.13[c]	6.3[c]
SbTeI			
SbSI	0.03[c]	0.20[c]	5.5[c]
SbSeI			

[a] Ref. 44. [b] Ref. 19. [c] Ref. 45.

highest calculated thermal conductivity, based on relaxation time, is 4.5×10^{14} W m^{-1} K^{-1} for YSeBr and 4.0×10^{14} W m^{-1} K^{-1} for YSeCl. A reduced effective mass of the charge carriers in YSeBr as compared to YSeCl can result in an increased carrier mobility, which raises the electronic thermal conductivity. The effective mass regulates how quickly the electrons can be accelerated in an electric field, and the low effective mass usually results in greater mobility. This suggests that in YSeBr, the electrons can carry heat more efficiently, and this results in a greater κ_e. When the temperature increases, some more charge carriers may get thermally stimulated, and the energy carried by these carriers rises. The increase in κ_e with temperature in YSeBr implies that the material can still transmit heat efficiently *via* electrons at greater temperatures. The higher κ_e at 850 K suggests that YSeBr has better thermal transport capabilities at higher temperatures than YSeCl, presumably due to a better balance of carrier mobility and scattering processes.

In Fig. 5(d), the specific heat capacity, C_v, is shown for YSeCl and YSeBr as a function of temperature. With increasing temperature, C_v increases, which can be explained by lattice dynamics and phonon contributions to thermal energy. At low temperatures, only the lowest-energy phonon modes (long-wavelength vibrations) are excited since the thermal energy is insufficient to excite higher-energy modes. As the temperature rises, more phonon modes are activated, adding to the specific heat. There is not much of a difference between the two materials. At most temperatures, YSeBr has a somewhat greater heat

capacity, which may have an impact on thermal management in certain applications, *e.g.* at 850 K, YSeBr has a specific heat capacity of 3.2, and YSeCl has 2.8. As phonon frequencies vary with atomic mass, heavier atoms result in lowering the frequency of phonon vibrations, allowing more phonon modes to be activated at a given temperature in YSeBr, resulting in a somewhat greater specific heat capacity.

The figure of merit is considered a significant metric in assessing the effectiveness of thermoelectric materials. Fig. 5(e) shows an increase in ZT from 50 K to 850 K for YSeCl and YSeBr, where YSeCl has a higher ZT value than YSeBr. Table 3 shows that our computed ZT values at 300 K are consistent with previously reported results, indicating the thermoelectric performance trends of these materials. The greater magnitude of the Seebeck coefficient in YSeCl as compared to YSeBr at 850 K would result in a higher ZT value. The reported ZT values for YSeCl (0.8) and YSeBr (0.7) at 850 K indicate the upper bounds or the "electronic ZT" approximations rather than fully converged total ZT values. These ZT values are rather an indicator of the two material's relative thermoelectric potential employing the electronic-only approximation. The higher ZT in YSeCl is also owing to a somewhat better carrier mobility, or a more advantageous carrier concentration, resulting in higher electrical conductivity at high temperatures than YSeBr. The lower thermal conductivity of YSeCl at high temperatures would also contribute to the higher ZT than YSeBr. YSeCl may display stronger anharmonic behaviour than YSeBr due to its smaller mass and stronger bonding, resulting in increased phonon dispersion and minor thermal conductivity. The Electronic susceptibility (χ) quantifies the response of a material to an electric field based on its electronic structure. It is determined by the number and kind of free carriers (electrons or holes) in the material, as well as its electronic structure. Fig. 5(f) indicates that the electronic susceptibility values for YSeCl and YSeBr are 4.8×10^{-12} m^3 mol^{-1} and 4.57×10^{-12} m^3 mol^{-1}, respectively, at 50 K. These values decline sharply from 50 K to 150 K and remain essentially constant up to 850 K. At low temperatures (around 50 K), many materials experience a reduction in the number of free charge carriers because they become "trapped" in impurity or localized states. As the temperature rises (from 50 K to 150 K), these carriers receive enough thermal energy to escape from their confined states, contributing to conduction and lowering the overall electronic susceptibility. Following the initial steep reduction, most thermally activated or delocalized carriers will be in a "free" state. Further, as seen in Fig. 5(f), increasing the temperature will not considerably increase the number of free carriers, resulting in a constant susceptibility value.

4 Conclusions

In this work, the electronic, optical, and thermoelectric transport properties of novel YSeM (M = Cl, Br) ternary chalcohalides were investigated using density functional theory. The results suggest that YSeCl holds potential for applications in optoelectronic devices due to its relatively wide direct band gap (2.69 eV, HSE06) and could also be attractive for applications requiring efficient electron–hole pair production and recombination. The smaller (direct) band gap (2.18 eV, HSE06) of YSeBr is attributed to bromine's lower electronegativity and its larger atomic radius, making it suitable for applications requiring lower-energy photon absorption. The calculated cohesive energy is −3.759 eV and −2.278 eV for YSeCl and YSeBr, respectively. For energies below 2.0 eV, YSeBr has a higher real dielectric constant, and respectively a larger refractive index and reflectivity as compared to YSeCl, while the imaginary part is close to zero for both materials in this energy range. Compared to YSeCl, YSeBr exhibits slightly greater absorption at low energies (2–4 eV), while at higher energies, the absorption coefficient increases and attains a maximum value of around 8.6 eV for both YSeCl and YSeBr, which is attributed to interband transitions. Concerning the thermoelectric properties, due to the improved mobility and the reduced effective carrier mass, YSeBr possesses a higher electronic thermal conductivity, resulting in the effective heat transfer at high temperatures. YSeCl also shows a stronger electrical conductivity, possibly a result of the better concentration of carriers or mobility, and consequently a greater figure of merit. Overall, YSeCl is predicted to be better suited for the thermoelectric applications, whereas the YSeBr is appropriate for high-temperature thermal control. The present study would pave the way for further fundamental investigations of the optoelectronic and thermoelectric properties of these semiconductors in nanoscale regimes for solar energy harvesting.

Conflicts of interest

The authors declare that they have no known competing financial interests or personal relationships that could have appeared to influence the work reported in this paper.

Data availability

The data that support the findings of this study are available from the corresponding author upon reasonable request.

Acknowledgements

This work was supported and funded by the Deanship of Scientific Research at Imam Mohammad Ibn Saud Islamic University (IMSIU) (grant number IMSIU-DDRSP2503).

References

1 G. R. Štrbac, S. R. Lukić-Petrović, D. D. Strbac, V. Benekou, A. Chrissanthopoulos and S. N. Yannopoulos, *J. Phys. Chem. B*, 2020, **124**, 2950–2960.
2 S. Sheokand, D. S. Ahlawat and V. Sheokand, *Micro Nanostruct.*, 2024, **190**, 207841.
3 R. Baghdad, *Micro Nanostruct.*, 2024, **186**, 207735.
4 D. C. Hvazdouski, M. S. Baranava, E. A. Korznikova, A. A. Kistanov and V. R. Stempitsky, *2D Mater.*, 2024, **11**, 025022.
5 M. Nowak, B. Kauch, P. Szperlich, M. Jesionek, M. Kępińska and Ł. Bober, *Ultrason. Sonochem.*, 2009, **16**, 546–551.

6 A. Audzijonis, R. Sereika, V. Lapeika and R. Žaltauskas, *Phys. Status Solidi B*, 2007, **244**, 3260–3264.
7 K. Nejezchleb and J. Horák, *Czech J. Phys.*, 1968, **18**, 138–142.
8 M. Nowak, P. Szperlich, Ł. Bober, J. Szala, G. Moskal and D. Stróż, *Ultrason. Sonochem.*, 2008, **15**, 709–716.
9 A. Audzijonis, L. Žigas, J. Siroic, A. Pauliukas, R. Žaltauskas and A. Čerškus, *Phys. Status Solidi B*, 2006, **243**, 610–617.
10 J. Palepu, P. P. Anand, P. Parshi, V. Jain, A. Tiwari, S. Bhattacharya, S. Chakraborty and S. Kanungo, *Micro Nanostruct.*, 2022, **168**, 207334.
11 S.-C. Hyun, Y.-G. Kim, M.-Y. Kim, J.-D. Koh, B.-S. Park and W.-T. Kim, *J. Mater. Sci.*, 1995, **30**, 6113–6117.
12 B. K. Vainshtein, V. M. Fridkin and L. A. Shuvalov, *Sov. Phys. Usp.*, 1968, **10**, 600–601.
13 R. Nitsche and W. J. Merz, *J. Phys. Chem. Solids*, 1960, **13**, 154–155.
14 P. Kichambare, *Solid State Ionics*, 1997, **101–103**, 155–159.
15 A. G. Papazoglou and P. J. Rentzeperis, *Cryst. Mater.*, 1983, **165**, 159–168.
16 X. Ou, C. Yang, X. Xiong, F. Zheng, Q. Pan and C. Jin, *Adv. Funct. Mater.*, 2017, **27**, 1606242.
17 Y. Tian, G. Li, Y. Zhang, D. Luo, X. Wang and Y. Zhao, *Adv. Mater.*, 2019, **19**, 1904876.
18 P. M. Fourspring, D. M. DePoy, T. D. Rahmlow Jr, J. E. Lazo-Wasem and E. J. Gratrix, *Appl. Opt.*, 2006, **45**, 1356.
19 A. Bafekry, M. Faraji, M. M. Fadlallah, D. M. Hoat, H. R. Jappor and I. A. Sarsari, *Phys. Chem. Chem. Phys.*, 2021, **23**, 25866–25876.
20 A. Audzijonis, R. Sereika, V. Lapeika and R. Žaltauskas, *Phys. Status Solidi B*, 2007, **244**, 3260–3264.
21 A. C. Wibowo, C. D. Malliakas, Z. Liu, J. A. Peters, M. Sebastian and D. Y. Chung, *Inorg. Chem.*, 2013, **52**, 7045–7050.
22 T. Das and S. Datta, *Nanoscale Adv.*, 2020, **2**, 1090–1104.
23 X. Li, Y. Dai, Y. Ma, S. Han and B. Huang, *Phys. Chem. Chem. Phys.*, 2014, **16**, 4230.
24 M. J. Varjovi, M. E. Kilic and E. Durgun, *Phys. Rev. Mater.*, 2022, **6**, 34004.
25 W.-Z. Xiao, H.-J. Luo and L. Xu, *J. Phys. D: Appl. Phys.*, 2020, **53**, 245301.
26 D. C. Hvazdouski, M. S. Baranava and V. R. Stempitsky, *IOP Conf. Ser. Mater. Sci. Eng.*, 2018, **347**, 012017.
27 H.-Q. Xu, G. Xiao, W.-Z. Xiao and L.-L. Wang, *Micro Nanostruct.*, 2022, **170**, 207396.
28 U. V. Ghorpade, M. P. Suryawanshi, M. A. Green, T. Wu, X. Hao and K. M. Ryan, *Chem. Rev.*, 2022, **123**, 327–378.
29 J. N. Wilson, J. M. Frost, S. K. Wallace and A. Walsh, *APL Mater.*, 2019, **7**, 010901.
30 K. T. Butler, J. M. Frost and A. Walsh, *Energy Environ. Sci.*, 2015, **8**, 838–848.
31 N. T. Hahn, A. J. Rettie, S. K. Beal, R. R. Fullon and C. B. Mullins, *J. Phys. Chem. C*, 2012, **116**, 24878–24886.
32 A. M. Ganose, K. T. Butler, A. Walsh and D. O. Scanlon, *J. Mater. Chem. A*, 2016, **4**, 2060–2068.
33 A. M. Ganose, S. Matsumoto, J. Buckeridge and D. O. Scanlon, *Chem. Mater.*, 2018, **30**, 3827–3835.
34 Z. Ran, X. Wang, Y. Li, D. Yang, X.-G. Zhao and K. Biswas, *npj Comput. Mater.*, 2018, **4**, 14.
35 X. Luo, L. Pan, T. Zhang, C.-E. Hu, Y. Cheng and H.-Y. Geng, *Mater. Sci. Semicond. Process.*, 2023, **166**, 107759.
36 G. Kresse and J. Furthmüller, *Phys. Rev. B Condens. Matter*, 1996, **54**, 11169–11186.
37 G. Kresse and D. Joubert, *Phys. Rev. B Condens. Matter*, 1999, **59**, 1758–1775.
38 J. P. Perdew, K. Burke and M. Ernzerhof, *Phys. Rev. Lett.*, 1996, **77**, 3865–3868.
39 J. Heyd, G. E. Scuseria and M. Ernzerhof, *J. Chem. Phys.*, 2006, **124**, 219906.
40 R. d. L. Kronig, *J. Opt. Soc. Am.*, 1926, **12**, 547.
41 G. K. H. Madsen and D. J. Singh, *Comput. Phys. Commun.*, 2006, **175**, 67–71.
42 M. Al-Hmoud, B. Gul, M. S. Khan, M. AlGharram, S. M. Aziz, T. Al Zoubi and A. M. Ahmed, *RSC Adv.*, 2025, **15**, 34808–34820.
43 S. Lee, K. Esfarjani, T. Luo, J. Zhou, Z. Tian and G. Chen, *Nat. Commun.*, 2014, **5**, 3525.
44 D. M. Hoat, D. K. Nguyen, V. V. On, J. F. Rivas-Silva and G. H. Cocoletzi, *Optik*, 2021, **244**, 167438.
45 W. Khan, S. Hussain, J. Minar and S. Azam, *J. Electron. Mater.*, 2017, **47**, 1131–1139.
46 H. Koc, S. Palaz, A. M. Mamedov and E. Ozbay, *Ferroelectrics*, 2017, **511**, 22–34.